PNAS RESEARCH ARTICLE | PHYSICS

Field-mediated locomotor dynamics on highly deformable surfaces

Shengkai Li[a,1], Yasemin Ozkan-Aydin[b,1], Charles Xiao[c], Gabriella Small[d], Hussain N. Gynai[a], Gongjie Li[a], Jennifer M. Rieser[e], Pablo Laguna[f], and Daniel I. Goldman[a,2]

Edited by Robert Austin, Princeton University, Princeton, NJ; received July 30, 2021; accepted June 2, 2022

Studies of active matter—systems consisting of individuals or ensembles of internally driven and damped locomotors—are of interest to physicists studying nonequilibrium dynamics, biologists interested in individuals and swarm locomotion, and engineers designing robot controllers. While principles governing active systems on hard ground or within fluids are well studied, another class of systems exists at deformable interfaces. Such environments can display mixes of fluid-like and elastic features, leading to locomotor dynamics that are strongly influenced by the geometry of the surface, which, in itself, can be a dynamical entity. To gain insight into principles by which locomotors are influenced via a deformation field alone (and can influence other locomotors), we study robot locomotion on an elastic membrane, which we propose as a model of active systems on highly deformable interfaces. As our active agent, we use a differential driven wheeled robotic vehicle which drives straight on flat homogeneous surfaces, but reorients in response to environmental curvature. We monitor the curvature field–mediated dynamics of a single vehicle interacting with a fixed deformation as well as multiple vehicles interacting with each other via local deformations. Single vehicles display precessing orbits in centrally deformed environments, while multiple vehicles influence each other by local deformation fields. The active nature of the system facilitates a differential geometry–inspired mathematical mapping from the vehicle dynamics to those of test particles in a fictitious "spacetime," allowing further understanding of the dynamics and how to control agent interactions to facilitate or avoid multivehicle membrane-induced cohesion.

active matter | terradynamics | elasticity | emergent phenomena

Significance

The study of how the environment influences movement is of interest in robotics, active matter physics and biology. While principles governing locomotion and control in individuals and collectives are well studied in hydro- and aerodynamic contexts, relevant interactions at highly deformable interfaces are less understood. We focus on a model system, a differential driven vehicle traversing an elastic membrane, studying the orbital dynamics of the vehicle influenced by an imposed curvature field and the dynamics and control of multiple vehicles reciprocally interacting via local surface deformations. The active nature of the system permits a mapping of the dynamics to a fictitious "spacetime," facilitating understanding of the orbital interactions and inspiring a control scheme that prevents or enhances multi-body cohesion.

The study of systems composed of internally driven agents has long been the domain of biology (1–3) and robotics (4–7) but is coming into vogue in physics in the field of active matter (8–10). Individual active agents display novel dynamics as well, largely a function of their persistent dynamics (11) and control (12). Active collectives display fascinating properties that nonactive systems do not; for example, collectives can show phase transitions (13) and drive force induced by a self-generated field (14). Active collectives can interact via physical (wakes in fluids) and social forces (15). And aerodynamic (16), hydrodynamic (17), and even terradynamic (18, 19) interactions in the bulk are well explored and increasingly understood in terms of their effects on agent locomotion such that we can build capable devices (20, 21) and create capable swarms (4–6, 22, 23).

In contrast, interactions in which locomotors move on an environment which is highly, but not necessarily permanently, deformed by the locomotor such that the environmental deformation field plays an important role in the locomotion and noncontact interactions are much less understood and are relevant in many active systems across environments. Such interactions most commonly occur at interfaces like on the surface of fluids, for example, in colloidal particles on fluid surfaces (24, 25), and water-walking and meniscus-climbing insects and robots (12, 26). But such dynamics can also be important in terradynamic situations such as interfaces composed of flowable granular media (18, 27) and mud [e.g., shear thickening substrates (28)], elastic surfaces such as leaf litter (29) and compliant trackways (30–33), or environments with obstacles of varying flexibility (34–37). In addition, systems in highly deformable environments have the feature that agents (spiders in webs, proteins in membranes) can sense and influence other entities without direct contact (38–40). Better understanding of such interactions could lead to global control of multiple agents via local sensing of field interactions alone (14, 22, 41, 42).

To avoid the time- and space-dependent complexity of hydrodynamic and complex terradynamic surfaces (e.g., splashing and permanent deformation, respectively), we chose, as a model system, an elastic membrane to study interaction of locomotor(s) on highly deformable environments. Specifically, we study the locomotion and field interaction of vehicles on highly deformable elastic environments via the study of two cases:

Author contributions: S.L., Y.O.-A., P.L., and D.I.G. designed research; S.L., Y.O.-A., C.X., G.S., H.N.G., P.L., and D.I.G. performed research; S.L. and P.L. contributed new reagents/analytic tools; S.L. and Y.O.-A., analyzed data; and S.L., Y.O.-A., G.L., J.M.R., P.L., and D.I.G. wrote the paper.

The authors declare no competing interest.

This article is a PNAS Direct Submission.

[1]S.L. and Y.O.A. contributed equally to this work.

[2]To whom correspondence may be addressed. Email: daniel.goldman@physics.gatech.edu.

This article contains supporting information online at https://www.pnas.org/lookup/suppl/doi:10.1073/pnas.2113912119/-/DCSupplemental.

Published July 20, 2022.

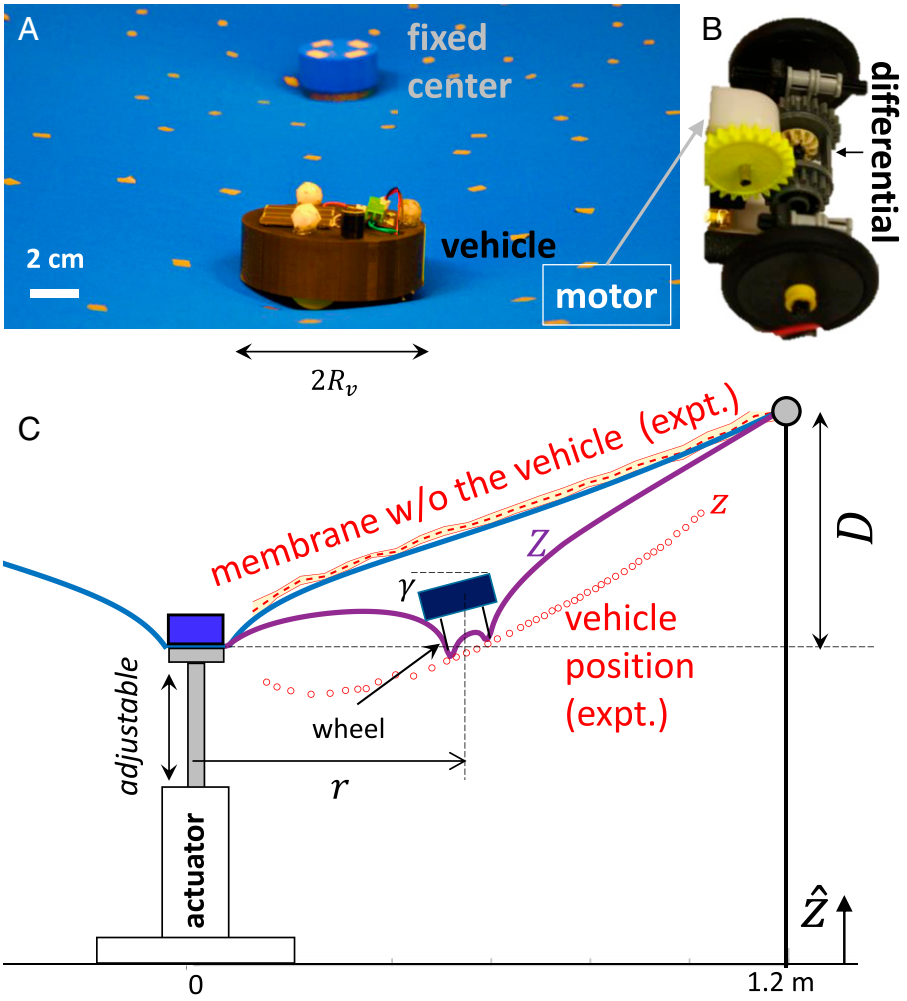

Fig. 1. Interaction induced by elastic substrate deformation. (*A*) One vehicle transiting around a central depression. (*B*) Side view of the differential driven vehicle and side view of the drive mechanism; see also Fig. 3*A* for more details. (*C*) Cross-section of the experimental setup with a depression D (z axis of the membrane is linearly stretched for visual clarity). The red dashed line denotes the measurement of the membrane shape in the absence of the vehicle; the red open dots show the contact positions of the vehicle with the membrane when it is placed at different radii. The vehicle's vertical position z relative to the confining outer membrane ring is approximated by the average of the membrane height Z around it: $z(\mathbf{r}) \approx \langle Z(\mathbf{r}') \rangle_{|\mathbf{r}'-\mathbf{r}|=R_v}$, where $\mathbf{r}$ and $\mathbf{r}'$ are the horizontal positions of the vehicle and the membrane around it. In the axisymmetric case shown here, it can be further approximated by $z(r) \approx (Z(r - R_v) + Z(r + R_v))/2$.

a single vehicle in the presence of a fixed obstacle and multiple vehicles influencing each other. We find that the dynamics of even a single vehicle are interesting when influenced by a nonmoving boundary via membrane curvature alone. Despite possessing neither sensing nor control, the vehicle orbits, collides with the center, or escapes from the membrane, analogous to how bodies orbit stars. We then show how multiple vehicles generically display a substrate-mediated cohesion whose collision timescale depends on vehicle mass, which is reminiscent of the Cheerios effect (43). Inspired by the response of the vehicle to curvature, we develop controllers which can help avoid such cohesion via local measurements of tilt, thus indeed generating global control over local forcing. We posit that the reciprocal coupling of the robot and the deformable substrate analyzed in detail here could be useful as a starting point for understanding field-mediated locomotor dynamics in more-complex environments.

Active Agent on Membrane: Field-Mediated Interaction from a Fixed Object

We first study the dynamics of a differential driven vehicle self-propelling on a deformable curved surface. The vehicle (Fig. 1*A* and *B*) takes inspiration from many active-matter experiments (25, 44, 45) and simulations (25, 46, 47) in that it moves straight in the absence of interaction with the other agents. Further, its mechanics are key elements of modern wheeled vehicles, which are deployed in diverse terradynamic scenarios, from paved roads to Martian landscapes (48–50). The vehicle has two rear wheels and one front spherical caster for stability. A critical feature of the vehicle is a differential (51) which allows independent rotation of the wheels upon different load conditions by maintaining constant speed governed by motor rotation rate. If the load of the two wheels is equal, for example, the vehicle is on level ground, both wheels turn at the same rate, and the vehicle goes straight. If the load of one of the wheels increases (i.e., vehicle tilts), the corresponding wheel slows down, and the opposite wheel speeds up, which results in turning motion around the slow wheel. While we have used a particular robot to perform the study, we note that constant speed motion is a convenient starting point to study more-general dynamics in such active systems.

Experiments were performed on a four-way stretchable spandex fabric (that stretches and recovers both width wise and lengthwise) affixed, unstretched, to a circular metal frame (see *Materials and Methods*) with a radius of $R = 1.2$ m. In the first situation with

a fixed center, a linear actuator attached to the center of the membrane warps the fabric from underneath to allow adjustable central depression of depth D with a cap (radius $R_0 = 5$ cm) fastening the actuator to the fabric. A diagram of the experimental setup is given in Fig. 1*C*. The membrane has a measured axisymmetry such that the SD of the membrane height at each radius is less than 5% of the central depression magnitude D (*SI Appendix*, section S6.2).

Three aspects are important to understand the dynamics of the vehicle on the membrane. The first is that the vehicle dynamics are highly damped, and inertia plays a minimal role: If the motor stops, the vehicle rapidly comes to rest (within a second). That is, there is no "rolling downhill." The second aspect is that the differential in the vehicle allows it to turn dynamically according to the local curvature instead of simply following the spatial geodesics of the membrane, which leads to almost straight trajectories given the shallow depressions of the membrane (*SI Appendix*, section S3). The third important aspect is that, while the global shape of the membrane without the vehicle is important, due to the vehicle's mass, its local environment deviates from the unloaded shape of the membrane, introducing an additional local deformation of the membrane. This results in a vehicle tilting to an angle γ (between the normal of the vehicle surface and $\hat{z}$) depending on the vehicle's radial position in membrane as depicted in Fig. 1*C*.

For simplicity, we first study the dynamics of a single vehicle moving at constant speed on the membrane (set by constant motor rotation rate and enforced by the differential mechanism). Experiments were conducted by setting the initial radius r (the distance between the center of the vehicle and the actuator) and heading angle θ (the angle between the radial direction and the velocity of the vehicle; Fig. 2*B*). The trajectories of the vehicle were recorded for 2 min by a high-speed motion capture system (Optitrack, 120 Hz) positioned above the membrane. Certain initial conditions (a particular radius $r_0 = r_c \approx 0.6$ m and heading $\theta_0 \approx 90°$) developed immediate circular orbits (Fig. 2*A*). However, similar to orbiting droplets on a liquid surface curved by their weight (52), for a majority of (r_0, θ_0), we observed trajectories consisting of retrograde precessing ellipse-like orbits (Fig. 2*B*) about the central depression; that is, the maximum radius of the orbit does not return to the same azimuthal position but rather lags behind after an orbit.

The precessing dynamics can persist for many orbits until the vehicle's orbit either slowly increases or decreases its eccentricity. In the former case, the vehicle ultimately collides with the central cap or escapes to the boundary. In the latter case, the precession decays into an approximately circular orbit with a critical r_c radius depending on the central depression D. From analysis of the vehicle mechanism and dynamics (*SI Appendix*, section S2), we attribute these behaviors to slight mechanical imperfections in the mass distribution in the vehicle, such as the deviation of the center of mass from the center line, ΔB. The eccentricity evolves over orbits with a factor $e^{-\epsilon\varphi/2}$, where $\epsilon = -\Delta B/L_c$; the precessing dynamics can be observed over longer timescales as the magnitude of imperfection decreases. Here L_c is the distance between the wheel axle and the center of mass. Ideally, a perfect vehicle with $\Delta B = 0$ makes $e^{-\epsilon\varphi/2}$ remain at one, and the orbit stays in the steady state forever. The half-life $(2\log 2)/\epsilon$ characterizes how steady an orbit is; the sign of ΔB determines whether the eccentricity will expand or decay. Besides the slight chirality characterized by ΔB, the slight anisotropy of the membrane could be another contribution to the variability of trajectories by generating a perturbation with period 2π in the azimuthal angle. This has a larger effect on lighter vehicle, since smaller mass is more susceptible to the same perturbation from anisotropy.

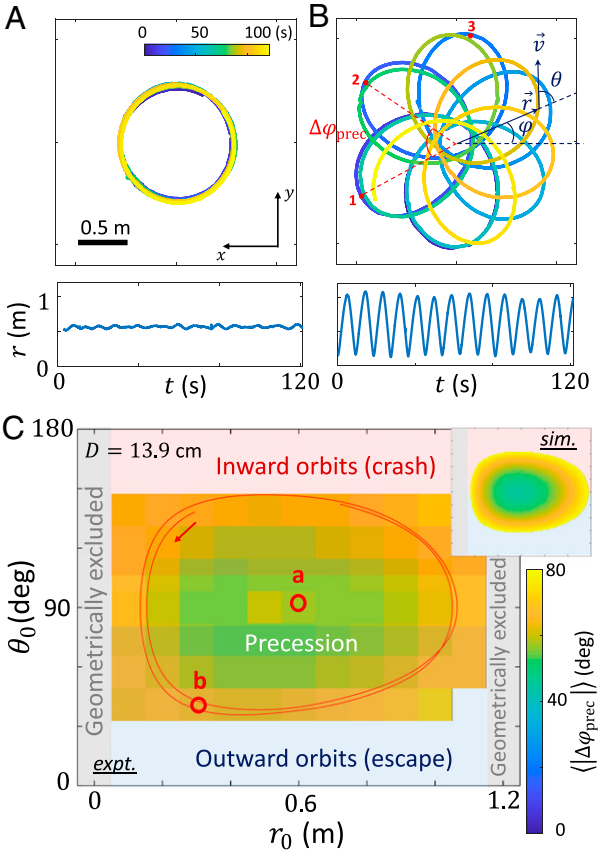

Fig. 2. Examples of bound vehicle trajectories. An example (*A*) circular orbit (Movie S1) and (*B*) eccentric orbit for the central depression $D = 13.9$ cm (Movie S2). In *B*, the angle θ denotes the heading angle, and φ denotes the azimuthal angle. The corresponding evolution of the radius over time is shown below. The eccentric orbit exhibits a precession of $|\Delta\varphi_{\rm prec}| \approx \pi/3$ evaluated from consecutive apoapsis or periapsis (peaks or valleys on the $r - t$ plots). (*C*) Precession angle's dependence on initial condition. The initial condition of the circular orbit (*A*) is indicated by a red circle. Any points on the trajectory of *B* can be considered as an initial condition of it. Two orbits of *B* are shown in a red curve. *Inset* shows the prediction from theory using Eqs. **1** and **2**; axes ranges are the same as those in the main figure.

To gain insight into the precessing dynamics, for bounded steady-state trajectories with half-lives of eccentricity longer than five revolutions, we measured average precession $|\Delta\varphi_{\rm prec}|$ as a function of initial conditions (r_0, θ_0) by evaluating the change in angular location of consecutive apoapsides or periapsides (e.g., between periapsides 1 and 2 in Fig. 2*B*). A map of this is shown in Fig. 2*C* in the r–θ space. We choose the heading angle θ rather than the azimuthal angle φ, to reduce the redundant counting of the same trajectories shifted by just an azimuthal angle due to the axisymmetry. We find the precession angle to be constant throughout the trajectory; therefore, all the points sampled from a trajectory share a constant precession angle, and each point's (r, θ) along this trajectory can be regarded as an effective initial condition in the trajectory r–θ space. Including these initial conditions, the map reveals that the precession is minimal when the vehicle is initiated at a particular radius r_c (0.6 m when the central depression $D = 13.9$ cm) and heading of 90°; $|\Delta\varphi_{\rm prec}|$ increased as initial conditions deviated from this region. However, r_0 is restricted to the range 0.2 m $\leq r_0 \leq$ 1.1 m to exclude the central cap in the membrane and to avoid starting the vehicle too close (less than 10 cm) to the outer ring. Initial headings which pointed approximately toward or away from the central depression did not achieve a stable orbit. While the range of θ_0 that starts stable orbits varies with r_0, we approximated the boundary of

stable orbits with uniform bounds of θ_0. That is, in experiments, for $\theta_0 < 30°$, the vehicle collided with the outer boundary, and, for $\theta_0 > 150°$, the vehicle crashed into the central cap.

Minimal Model for Vehicle Dynamics

To gain insight into how vehicle orbital dynamics emerge solely due to interaction with the curvature field generated by both the central depression and the vehicle's local depression field (Fig. 1*A*), rather than solving a coupled membrane–vehicle interaction system of equations, we instead construct a minimal model which gives physical insight into how such deformation fields influence the vehicle's dynamics. Since the vehicle moves at a constant speed, this model requires that the acceleration is perpendicular to the velocity such that $\Psi^2 a_r v_r + a_\varphi v_\varphi = 0$, where the projected components of acceleration in r and φ directions are $a_r = -a\, v_\varphi/(\Psi\, v)$, $a_\varphi = a\Psi v_r/v$. Here $\Psi^2 \equiv 1 + z'^2$, with $z' \equiv \partial z/\partial r$ as the gradient of the vehicle's height z measured from the frame holding the spandex sheet. With the help of $\cos\theta = \Psi\, v_r/v = \Psi\, \dot{r}/v$ and $\sin\theta = v_\varphi/v = r\dot{\varphi}/v$, we have

$$\frac{a_\varphi}{r} = \ddot{\varphi} + \frac{2\,\dot{r}\,\dot{\varphi}}{r} = \frac{a}{r}\cos\theta \qquad [1]$$

$$a_r = \ddot{r} - \frac{r\,\dot{\varphi}^2}{\Psi^2} + \frac{\Psi'}{\Psi}\dot{r}^2 = -\frac{a}{\Psi}\sin\theta, \qquad [2]$$

with $a = [\Psi^2 (a_r)^2 + (a_\varphi)^2]^{1/2}$. Dots and primes denote differentiation with respect to t and r, respectively. Our experiments reveal that, to a good approximation, the dependence of the vehicle's acceleration on the radius and heading is given by

$$a = k\, \sin\theta, \qquad [3]$$

Where k (referred to as the acceleration strength below) is a function of r only (Fig. 3*C*). We want to point out that the form of $k \sin\theta$ can be regarded as the first-order expansion of any $a(r, \theta)$ for any vehicles. Having $a \propto \sin\theta$ implies that, in this axisymmetric case, the magnitude of the acceleration is proportional to that of the cross-product between the velocity and the gradient of the terrain, since the gradient of the terrain is aligned with the radial direction. We will later show that $a \propto |\mathbf{v} \times \nabla z|$ also holds for surfaces with arbitrary shapes.

We treat the vehicle with tilt angle γ from its level orientation as driving on a local incline with slope γ. From a theoretical analysis of how the constant-speed differentially driven vehicle pivots on a slope (Fig. 3*B*; see *SI Appendix*, section S1 for derivations), we found that the acceleration strength $k = C\, g\, \sin\gamma\, \cos\gamma \approx C\, g\, |\nabla z|$ with g as Earth's gravity. The prefactor C is a mechanical constant related to the structure of the vehicle as $C = L_c^2/(L_c^2 + 1/2R_v^2)$, where $L_c \approx 1$ cm is the distance between the wheel axle and the center of mass (*SI Appendix*, Fig. S1), and $R_v = 5$ cm is the radius of the vehicle. The theoretical value for C from the model is ~0.074, while the experimental fit (Fig. 3*C*, *Inset*) gives a value of 0.073 ± 0.001 (*SI Appendix*, section S1).

The model as described by Eqs. **1** and **2** yields good agreement with experiments over a range of v = 0.20 m/s to 0.32 m/s. The essential ingredient of the model is that the differential mechanism ensures torque balance on both wheels. In addition, the rolling friction on the caster is negligible compared to other contact forces (see Fig. 3*A* for a force diagram). The model indicates $k = a/\sin\theta$ should be the same for any θ for a balanced vehicle. The experimentally measured result shows a slight dependence on heading angle θ (*SI Appendix*, Fig. S3) that can be understood as weight imbalance, characterized by ΔB. Introduction

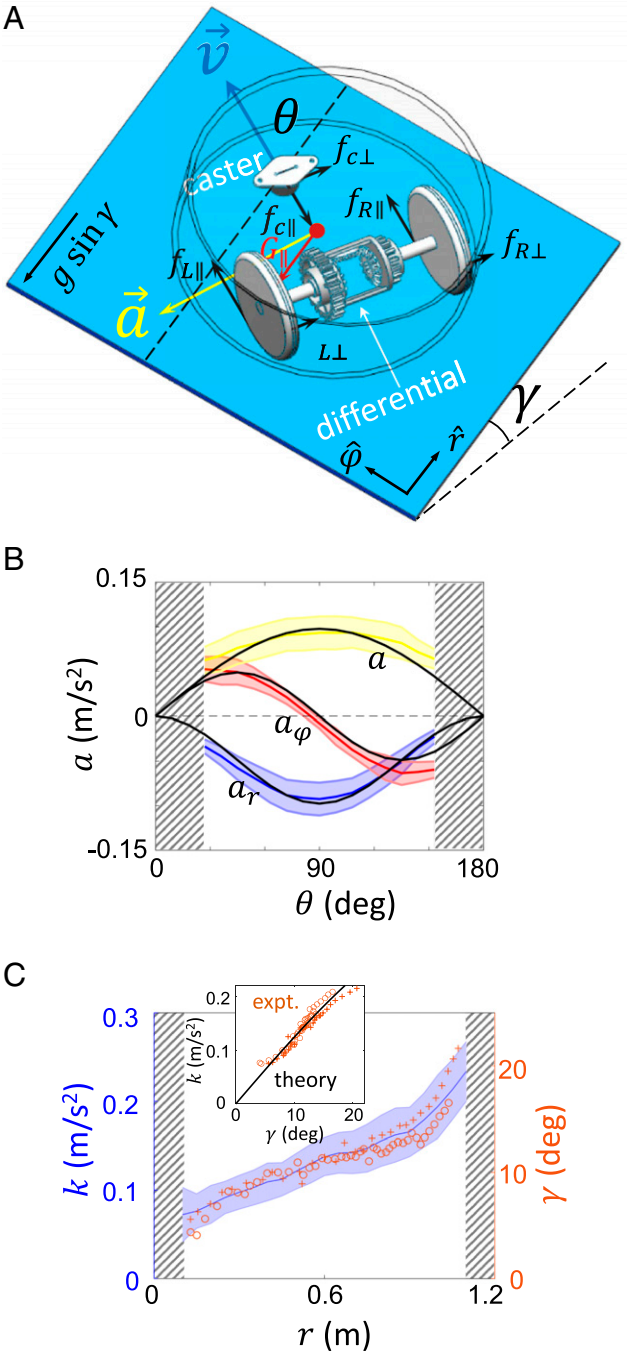

Fig. 3. Vehicle dynamics. (*A*) Schematic of a vehicle moving on a piece of membrane and its force diagram. The dashed line on the incline shows the radial direction. The frictions on the wheels and the caster are shown in black, and the component of Earth gravity along the slope is shown in red. (*B*) Magnitude of the acceleration a (yellow), and its components a_r (blue) and a_φ (red) as a function of the heading angle θ evaluated at $r = 0.3$ m (central depression $D = 9.6$ cm) obtained from 238 experiments. The colored solid lines and shading denote the mean and SD over the experiments. Black lines correspond to $a = k(0.3\text{m}) \cdot \sin\theta$, $a_r = -(a/\Psi)\sin\theta$, and $a_\varphi = a\cos\theta$, with $\Psi \approx 1$. The gray shaded regions indicate extreme headings that do not have steady trajectories. Data at other radii can be found in *SI Appendix*, Fig. S2. (*C*) The acceleration strength k and vehicle tilt γ as a function of the radius r for $\theta = 90°$, with the solid blue line and shading denoting the mean and SD of k obtained from 238 experiments. The red markers show the vehicle tilt γ measured from the experiment on two different azimuths separated by 90°, with open circles and pluses, respectively. *Inset* shows the relation between k and γ using the k data (mean) from the main figure and the theoretical curve $k = 0.074\, g \sin\gamma \cos\gamma$.

of this bias into the analysis returns a correction in the form of $a_{bias}/\sin\theta = k \cdot (\Delta B/L_c)\cot\theta$. It vanishes when $\theta = \pi/2$ or $\Delta B = 0$ (a perfectly balanced vehicle). Integration of Eqs. **1** and **2** yields precession dynamics that quantitatively matches with the experiments for all different depressions (Figs. 2*C* and 4*B*).

An important aspect of the dynamics which is revealed by the model is that, unexpectedly, the vehicle does not follow spatial geodesics of the membrane [as in the museum demos of general relativity (GR) (53)] given by curves on curvatures with metric $ds^2 = \Psi^2 dr^2 + r^2 d\varphi^2$. These spatial-only geodesics are nearly straight lines in our setup (*SI Appendix*, Fig. S4). We will later show that the essential ingredients that generate this difference are the deformation of membrane by the vehicle, and the active nature of the system shown in the vehicle's ability to change the direction of motion as a consequence of the local tilt of the vehicle. These two aspects are reflected, respectively, in the acceleration strength k governed by membrane deformation and θ, the heading angle of the vehicle.

Understanding and Manipulating Dynamics via Application of Differential Geometry

To understand aspects of the system's dynamics (e.g., how substrate parameters can alter orbital properties of the active locomotor), we sought to obtain conserved quantities including an effective potential. While there are many ways to obtain these quantities, inspired by features of the dynamics resembling those found in astrophysical systems, we chose to use techniques from differential geometry, the mathematics relevant to situations described by Einstein's theory of GR. In a separate paper (54), we further expand on the connections of our robophysical system to GR.

Our scheme proceeds in analogy to GR: Recall that, in GR, test particles move in response to the curvature of spacetime by following the locally length-minimizing curves (i.e., geodesics). Thus, we must first obtain the "metric" of the effective spacetime, which describes the spacetime curvature. Following the metric and applying the variational principle, one could obtain the equation of motion for the test particles (e.g., ref. 55). For instance, the Minkowski metric in the flat spacetime is defined by the diagonal matrix $\eta_{\alpha\beta} = \{-1, 1, 1, 1\}$ in Cartesian coordinates. This specifies that the distances between close points in spacetime can be calculated as the following—$ds^2 = -dt^2 + dx^2 + dy^2 + dz^2$—and leads to the equation of motion $d^2x^\alpha/dt^2 = 0$ for test particles. By matching the geodesics equations of the metric with the equations of motion Eqs. **1** and **2**, one can find that the metric is

$$ds^2 = -\alpha^2 dt^2 + \Phi^2(\Psi^2 dr^2 + r^2 d\varphi^2), \qquad [4]$$

where the curvatures are $\alpha^2 = E^2(1 - v^2 e^{-K/v^2})$ and $\Phi^2 = E^2 e^{-K/v^2}(1 - v^2 e^{-K/v^2})$. Here, $K = K(r) \equiv \int_0^r k(s)\Psi(s)ds$, and E is a constant of motion. The metric provides us with

$$1 = \frac{\Phi^2}{\alpha^2}\Psi^2\dot{r}^2 + \frac{1}{r^2}\frac{\alpha^2}{\Phi^2}\frac{L^2}{E^2} + \frac{\alpha^2}{E^2}, \qquad [5]$$

where L is another constant of motion. The details of derivation can be found in *SI Appendix*, section S4.

Eq. **5** can be rewritten in the following suggestive form: $\mathcal{E} = 1/2m\,\dot{r}^2 + V$, with $\mathcal{E} = 1/2$, $m = \Phi^2\Psi^2/\alpha^2$ as the effective mass, and $V = [\alpha^2\ell^2/(\Phi^2 r^2) + \alpha^2/E^2]/2$ as the effective potential, where we have defined $\ell \equiv L/E$. Plugging in the α^2 and Φ^2 derived above, we finally arrive at the effective potential

$$V = \frac{1}{2}\left(\frac{\ell^2}{r^2}e^{K/v^2} + 1 - v^2 e^{-K/v^2}\right). \qquad [6]$$

Note that the energy and angular momentum enter through the ratio $\ell = L/E$, which can be calculated from the initial conditions, since $\ell = \Phi^2 r^2\dot{\varphi}/\alpha^2$. Fig. 4*A* shows examples of the potential V for different values of ℓ with $\ell_{max} = v\ r_c \exp(-K(r_c)/v^2)$ (*SI Appendix*, section S4). The dashed line at $1/2$ denotes $\mathcal{E}$, and the turning points where $\dot{r}$ changes sign when the potential energy reaches the maximum amount are given by the solution to $r_\pm = \ell\, e^{K_\pm/v^2}/v$, where we use the subscript $\pm$ to denote a quantity evaluated at the turning points. Circular orbits occur when the minimum of the potential matches $\mathcal{E}$. The minimum is found from $V' = 0$ and is located at $r_c = v^2/k_c$, where $k_c \equiv k(r_c)$.

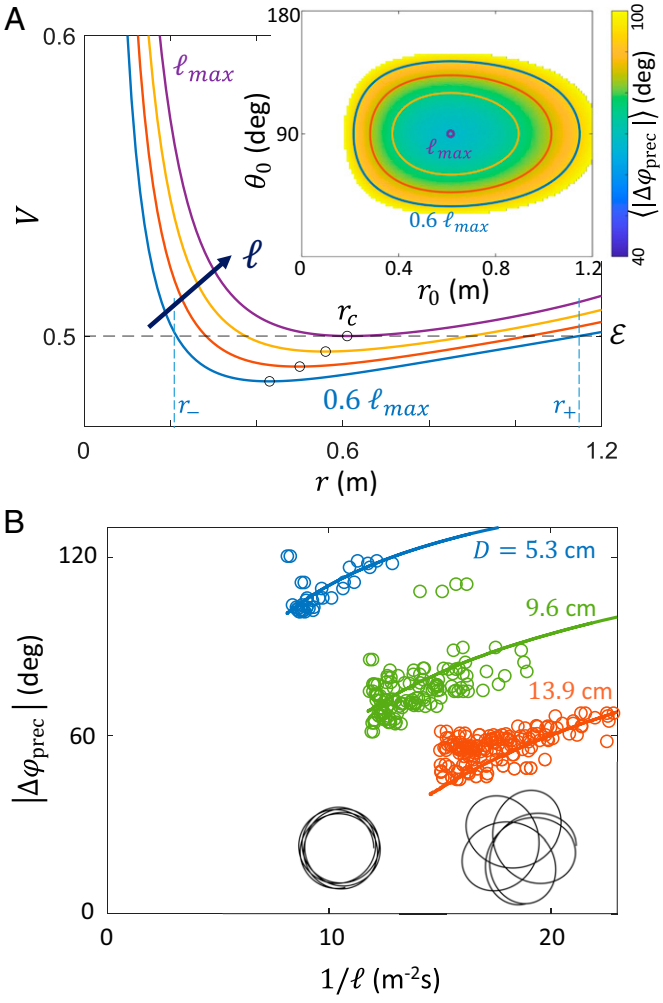

Fig. 4. The effective potential governing the orbital dynamics. (*A*) Simulation data of V is shown for different values of ℓ with $D = 9.6$ cm. Black dots denote the minimum point of a given potential curve, and $r_c = v^2/k_c$ labels the case of a circular orbits when $\mathcal{E} = V_c$. The corresponding trajectories in the r–θ space are shown in *Inset*. (*B*) Precession angle $|\Delta\varphi_{prec}|$ as a function of the effective initial radius r_0 for $\theta_0 = \pi/2$ and central depressions $D = 13.9$ cm (vermilion), 9.6 cm (green), and 5.3 cm (blue). Experimental data are open circles and plus signs. Solid lines are theoretical prediction using Eqs. **1** and **2**, or, equivalently, Eq. **7**. The open dots show the r_-, and the pluses show the r_+. *Insets* below the curves show the trajectories at different radii for $D = 9.6$ cm. Experimental observation of precession angle matches the theoretical value (from the solid lines in *A*) with an R^2 of 0.87.

With the effective potential discovered from the mapping scheme, we can now explain the dependence of orbital precession on initial conditions and system parameters. To begin, we introduce the definitions of E and L to eliminate $\dot{r}$ in $\mathcal{E} = 1/2m\,\dot{r}^2 + V$ in favor of $dr/d\varphi$. This results in

$$\frac{\ell^2}{r^2}\left[\frac{1}{r^2}\left(\frac{dr}{d\varphi}\right)^2 + 1\right] = v^2\, e^{-2K/v^2}. \qquad [7]$$

Next, we apply the change of variable $u = \ell/r$, and differentiate with respect to φ and get

$$\frac{d^2u}{d\varphi^2} + u = \frac{k\,\ell}{u^2} e^{-2K/v^2}. \qquad [8]$$

As noted above, for circular orbits $r_c = v^2/k_c$, or equivalently $u_c = k_c\,\ell/v^2$. Perturbing Eq. **8** about a circular orbit, that is, $u = u_c + \delta u$, we get

$$\frac{d^2\delta u}{d\varphi^2} + \left(1 + \frac{k_c'}{k_c} r_c\right)\delta u = 0. \qquad [9]$$

Thus, $\delta u \propto \cos(\omega\,\varphi)$ with $\omega^2 \equiv 1 + r_c\,k_c'/k_c$, where $k_c' \equiv k'(r_c)$, and the perturbative solution to Eq. **8** is then given by $u = u_c[1 + e\,\cos(\omega\,\varphi)]$, where e is the eccentricity of the orbit. Notice, from this solution, that one radial cycle takes place over a $2\pi/\omega$ angular cycle. Therefore, the precession angle is given by $\Delta\varphi_{\text{prec}} = 2\pi/\omega_c - 2\,\pi \approx -\pi\,r_c\,k_c'/k_c$. Since $k_c > 0$, the sign of $\Delta\varphi_{\text{prec}}$, namely, the direction of the precession, is given by the sign of k_c'. If $k_c' > 0$, we have $\Delta\varphi_{\text{prec}} < 0$, retrograde precession, with prograde precession if $k_c' < 0$. From Fig. 3*C*, we have that $k_c' > 0$, which explains the observed retrograde precession. Further, the dependence of $\Delta\varphi_{\text{prec}}$ on r_c is consistent with our observation that the magnitude of the apsidal precession ($\Delta\varphi_{\text{prec}} < 0$) decreases as the radius of the orbits approaches the radius of the circular orbit r_c.

We now reexamine the dependence of precession angle $\Delta\varphi_{\text{prec}}$ on initial conditions (Fig. 2*C*) in the mapping framework. We now can see that contours of constant color correspond to trajectories with the same angular momentum ℓ. And, notably, the precession angle decreases as the orbits become more circular, with $\Delta\varphi_{\text{prec}} = -\pi\,r_c\,k_c'/k_c$ for the circular orbit. Fig. 4*B* shows $\Delta\varphi_{\text{prec}}$ as a function of r_0 for initial heading angle $\theta_0 = 90°$ with both the experimental data and the solution to Eq. **7**. The minimum precession angle occurs for circular orbits.

As a consequence of $k' > 0$, our system generates retrograde orbits such that the vehicle's precession is opposite to that of GR in common situations. With our mapping, it is straightforward to understand how to obtain more GR-like prograde precession [like that of Mercury (56, 57)]: We must change the sign of the slope of k so that $k' < 0$ over a significant range of the vehicle trajectory. Because k is connected to the tilting angle γ, we can achieve the desired change by increasing the tension of the membrane or decreasing the mass of the vehicle to enable the vehicle to more closely track the imposed membrane shape.

We chose to change the mass of the vehicle and constructed a smaller, lighter vehicle with mass 45 g (Fig. 5*A*), approximately one-quarter that of the original vehicle in Fig. 1, a radius of 4 cm, and a speed $v = 0.11$ m/s. The vehicle produced trajectories (Fig. 5*C*) demonstrating prograde precession over all sampled initial conditions (65 total experiments). For a particular initial condition ($r_0 = 69$ cm, $\theta_0 = 90°$), four out of five trials produced precessing orbits with significant eccentricity; here

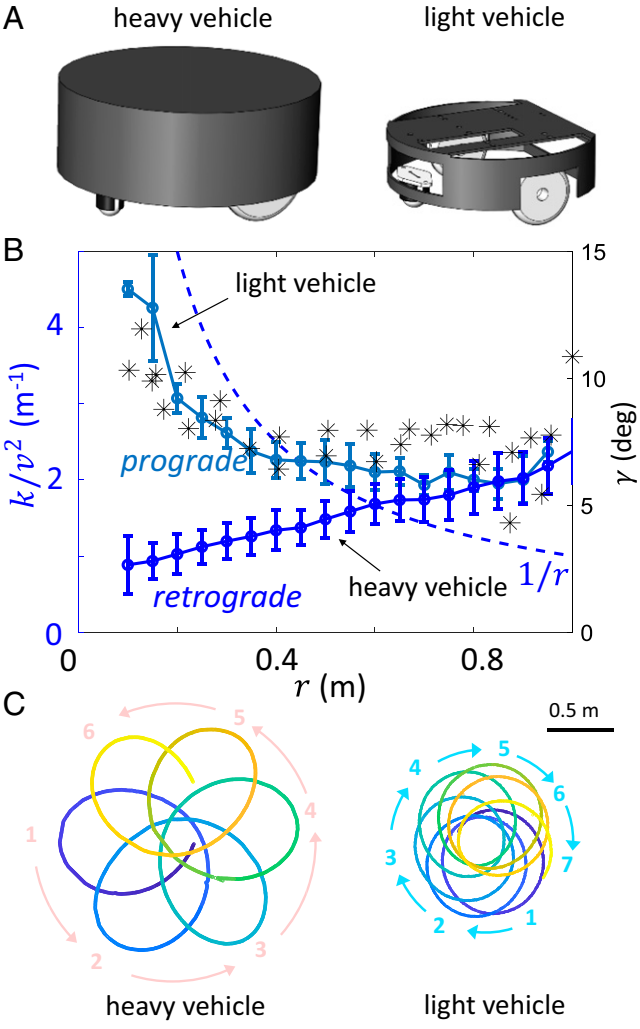

Fig. 5. Tuning the spacetime to generate prograde precession. (*A*) The heavy vehicle ($m \approx 160$ g) and the light vehicle ($m \approx 45$ g). (*B*) Different $k(r)$ functions for prograde (light blue) and retrograde (dark blue) precession measured from experiments. The light vehicle has a negative k' at r_c (the intersect of $k(r)/v^2$ and $1/r$), while the heavy vehicle has a positive k' at such an intersect. The decreasing k has the same trend as the measured tilt angle $\gamma(r)$ (black stars). (*C*) Clockwise trajectories with retrograde (*Left*) and prograde (*Right*) precessions from experiments. Perihelia are marked in order. The prograde precession is made by a lightweight vehicle on the membrane with $D = 17$ cm central depression, for initial conditions $r_0 = 20$ cm, $\theta_0 = 90°$. The periapsides numbered in blue show a clockwise order while the orbit is precessing in the same direction (for video, see Movie S3). The magnitude of the precession for this trial is $\Delta\varphi_{\text{prec}} = 51°$.

$\Delta\varphi_{\text{prec}} = +22° \pm 16°$. The theoretical prediction—with $k(r)$ (Fig. 5*B*) deduced from such trajectories—$\Delta\varphi_{\text{prec}} = +33° \pm 7°$ mostly overlaps with the experimental range. For a given initial condition, the lightweight vehicle showed greater trajectory variability than that of the heavier vehicle. We posit that such variability is related to the slight membrane anisotropy, which makes the dynamics of the lightweight vehicle sensitive to initial conditions. Here the change of precession sign with the vehicle's mass demonstrates how the matter reciprocally tells the local spacetime how to curve and influences its global dynamical properties.

Development of a Theory for Reciprocal Field-Mediated Interaction Dynamics

Thus far we have studied the interactions between a single vehicle and a central depression (which generates a time-independent imposed background) and have shown how we can understand

the field-mediated orbital dynamics by mapping them to a "spacetime" using techniques from study of relativistically orbiting bodies. There are situations in which the deformation field experienced by a vehicle could be time dependent; we have observed that a robot can be "guided" without contact via local deformation of the membrane alone (Movie S4). Further, in the case of swarms of vehicles moving on a curvature field, this sets up interesting dynamics such that (in the case of two robots for example) each robot carries its own depression field and affects another robot via this field alone, which could then affect the initial robot.

Therefore, we next sought to develop a theory for the interaction of two agents via fields alone. The first element of the theory requires that we develop an equation of motion for the dynamics of a single vehicle experiencing an imposed deformation field that is not necessarily at the center of the membrane (the spacetime telling matter how to move a component of the Wheeler encapsulation of the mechanics of GR). Thus, we need to first generalize the equations of motion (Eqs. **1** and **2**) to a vehicle on an arbitrary terrain. The axisymmetric model can be generalized for an arbitrary substrate by noticing that $a = k\ \sin\theta$, where θ is the angle between the velocity and the gradient of the slope, and k is the magnitude of the gradient multiplied by a mechanical constant. In the symmetric case, the gradient is always along the radial direction so that only the magnitude of the gradient $k = C\ g\ \sin\gamma\cos\gamma \approx C\ g\ |\nabla z|$ is needed. In the general case, noticing the $\sin\theta$ is the cross-product of the unit vectors of the arbitrary terrain gradient $\mathbf{d} = -\nabla z$ and the vehicle velocity, the generalized equation of motion (see *SI Appendix*, section S5 for derivation) is

$$\ddot{x} = C\ g\ \dot{y}\ (d_x\dot{y} - d_y\dot{x})/v^2 \qquad [10]$$

$$\ddot{y} = -C\ g\ \dot{x}\ (d_x\dot{y} - d_y\dot{x})/v^2. \qquad [11]$$

Conceptually, this is our "$F = ma$," with $\mathbf{d}$ playing the role of "F" (recall $d_i = -\nabla_i z$ with $i = x, y$).

To complete the field-mediated interaction picture, since a moving vehicle presents to another vehicle a time-dependent deformation field, we require an equation to describe how a vehicle (the "matter") deforms the membrane curvature.

To characterize how the membrane responds to local perturbations, we use the wave equation, the simplest equation for a membrane assuming linear elasticity,

$$\ddot{Z} - v_m^2\Delta Z = -P, \qquad [12]$$

where v_m is the speed of propagation of disturbances in the membrane, and $P = P_0\,(1 + \tilde{P})$, with $P_0(>0)$ as the force load from the membrane and $\tilde{P}$ as the additional load from the vehicles, which is the area density of the vehicles normalized by the area density of the membrane. Since P_0 is the stationary force load when the membrane is only deformed by its weight, the time dependence in the source in Eq. **12** arises from $\tilde{P}$ due to the moving vehicles. Experiments examining the membrane elasticity have found that the shape of a free stationary membrane where $\tilde{P} = 0$ and $\ddot{Z} = 0$ follows the Poisson equation reasonably well (*SI Appendix*, section S6).

The speed of propagation for the membrane in our experiment is $v_m \approx 400$ cm/s, which is significantly larger than the typical speed of our vehicles ($v \approx 20$ cm/s). Therefore, we neglect time derivatives in Eq. **12** and solve instead the Poisson equation $\Delta Z = P/v_m^2$.

Therefore, the evolution of the system proceeds as follows (Fig. 6*A*): Given the location of the vehicles, one first constructs the source P and solves $\Delta Z = P/v_m^2$ to obtain the membrane

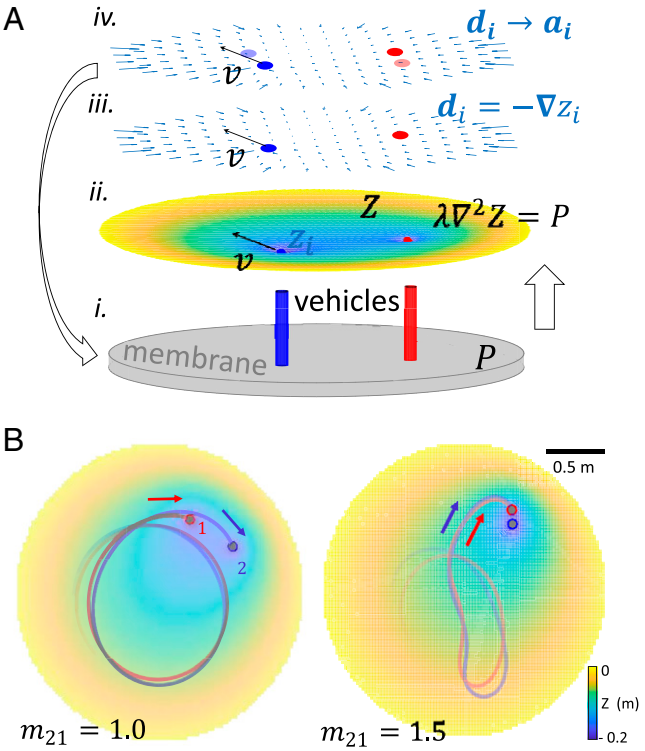

Fig. 6. Reciprocal interaction between the vehicle dynamics and curvature field. (*A*) A sketch of the simulation procedure: (*i*) First, the shape of the membrane is solved from the Poisson equation with the load indicated in the bottom: gray disk for the membrane and two colored posts for the two vehicles in this example. (*ii*) Then, the height profile of the vehicle is evaluated at its position. (*iii*) Afterward, the terrain gradient **d** is evaluated from the height profile of the vehicle. (*iv*) Finally, the acceleration determined by **d** using Eqs. **10** and **11** is integrated to update the new positions of the vehicles, and the computation goes back to the first step again. (*B*) Theory and simulation predict that a larger leader mass ratio ($m_{21} \equiv m_2/m_1 = 1.5$, where $m_1 = 150$ g) fosters a merger better than a smaller one ($m_{21} = 1.0$).

profile function Z (Fig. 7*C*). After Z is obtained, naively, one would use $Z(\mathbf{r})$ as the height of the vehicle $z(\mathbf{r})$. However, for a vehicle with a finite size, the actual physical contacts between the wheels and the membrane occur near the circumference of the disk. Thus, the vehicle height $z(\mathbf{r})$ can be approximated by the average membrane height $Z(\mathbf{r})$ around the disk circumference ($z(\mathbf{r}) \approx \langle Z(\mathbf{r}')\rangle_{|\mathbf{r}'-\mathbf{r}|=R_v}$; Fig. 1*C* and *SI Appendix*, section S7). On our circular membrane, the analytical solution to Z evaluated in z yields the vertical position z_i for vehicle i with mass m_i as

$$2\pi\lambda z_i = \frac{\pi}{2}(|\mathbf{r}_i|^2 - R^2) + \frac{m_i}{\sigma}\log\left(\frac{R_v R}{R^2 - |\mathbf{r}_i|^2}\right) + \frac{1}{\sigma}\sum_{j\neq i} m_j\left(\log\frac{|\mathbf{r}_i - \mathbf{r}_j|}{|\mathbf{r}_i - \mathbf{r}_j'|} - \log\frac{|\mathbf{r}_j|}{R}\right), \qquad [13]$$

where $\mathbf{r}_i, \mathbf{r}_i' = (R/|\mathbf{r}_i|)^2\mathbf{r}_i$ are the planar position of the ith vehicle and its image charge (58), R and R_v are the radii of the membrane and the vehicle, σ is the area density of the membrane, and $\lambda = v_m^2/P_0$ is a membrane constant; the three terms in the solution show, respectively, the contributions of the vehicle height field from the membrane, the weight of the vehicle of interest, and the other vehicles. The last term conceptually acts as an attractive potential (like the Newtonian gravitational potential), whose gradient generates a pairwise attractive force between the vehicles.

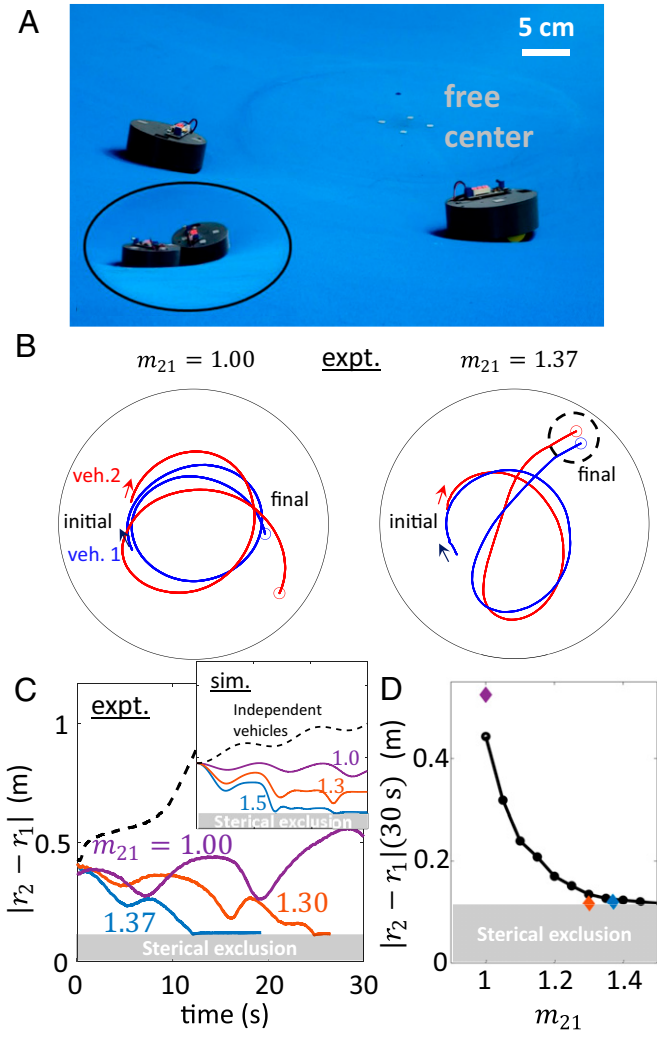

Fig. 7. Substrate deformation–induced cohesion. (*A*) Two vehicles moving on the elastic membrane merge due to the substrate-mediated attraction. The initial azimuth angle between the vehicles is 45°. The circled region in lower left shows position of two vehicles after 25 s. (*B*) Example trajectories of the two interacting vehicles with different mass ratio ($m_2/m_1 = m_{21} = 1.00$ and 1.37, where $m_1 = 150$ g) for a duration of 30 s. See Movie S5 for videos. (*C*) The evolution of the relative distance between the two interacting vehicles (solid line) compared to the noninteracting case (dashed line) where two vehicles with $m_{21} = 1.30$ were released individually from the same initial condition. The time to merge is shortened by the increased masses of the leading vehicle (vehicle 2, m_2). Conversely, the distance between two independent vehicles from the same initial condition is nondecaying. *Inset* has the same axis ranges as the main figure. (*D*) Simulation shows that the distance at 30 s between the two vehicles decays with the mass ratio m_{21}. Experiment results from *C* are shown in diamonds.

With z, and, therefore, the acceleration, as a function of the terrain gradient $-\nabla z$ at hand, one obtains the new position of the vehicles by integrating Eqs. **10** and **11**.

Attraction and Cohesion Dynamics in a Two-Vehicle System

While a full systematic study of interaction dynamics for arbitrary initial conditions of the two vehicles is beyond the scope of this work, integration of the above multibody dynamical model reveals that, surprisingly, the simulation does not predict strong attraction between two vehicles with the same mass at the same speed (Fig. 6*B*) unless they are started facing each other; experimental measurements of robot interaction are in accord with this prediction (Fig. 7*B* and *C*) such that two equally massed vehicles will undergo many transits around the membrane without cohering. This is analogous to the eccentric Kozai–Lidov mechanism, where the eccentricity excitation reduces when the masses become equal to each other and decreases the merger rate (59). In contrast, the simulation predicts that, in a situation where one vehicle trails another (Fig. 7), increasing the mass of the leading vehicle can increase the attraction (Fig. 6) and lead to vehicle merger (cohesion).

To test the hypothesized merger enhancement with the increase of the leading vehicle's mass, we experimentally increased the mass of the leading mass vehicle (small weights were attached to the top of the vehicle without changing the center of mass), m_2, relative to the trailing vehicle, m_1 (characterized by the mass ratio $m_{21} = m_2/m_1$, where $m_1 = 150$ g). For each experiment, both vehicles were placed at a radial distance of 60 cm from the center with azimuthal separation $\psi = 45°$ and both with a heading of $\theta = 90°$. Before each experiment, we set the speed of the two vehicles to 0.2 m/s by manually adjusting the voltage of the motors. Due to the finite voltage, the speed slightly drops ($< 10\%$) as the separation between the two vehicles decreases. Fig. 7*B* shows how the dynamics depend on the mass ratio. When $m_{21} = 1$, both vehicles execute nearly-circular orbits (Fig. 7*B*, *Left*) and generally do not merge in a short time (*SI Appendix*, section S8). As m_{21} is increased to 1.37, the trailing vehicle eventually becomes "captured" by the leading vehicle, leading to an effective cohesion such that the vehicles collide and then continue to move together for the duration of the experiment (Fig. 7*B*, *Right*).

To quantify the attraction and cohesion dynamics, we measured the Euclidean distance between the vehicles projected onto the horizontal plane, $|\mathbf{r}_1 - \mathbf{r}_2|$, as a function of time. We find that the time to capture is reduced as the mass of the leading vehicle increases (Fig. 7*C*). For instance, when $m_{21} = 1.30$, it takes around 25 s for the trailing vehicle to become captured (i.e., the vehicles collide when $|\mathbf{r}_1 - \mathbf{r}_2| = 2R_v$). When $m_{21} = 1.37$, this capture occurs significantly faster, with the vehicles colliding in about 12 s. The coupling effects are highlighted by contrasting to the dynamics from independently conducted single-vehicle experiments, one with the initial conditions of the "leading" vehicle and the other with the initial conditions of the "trailing" vehicle. The distance evaluated from these two independent trajectories shows a nondecaying trend that differs from the cases with both vehicles on the membrane (dashed lines in Fig. 7*C*). Simulations using the same setup as the experiments show qualitative match with the experiments, and the distance between the two vehicles decreases with the mass ratio m_{21} (Fig. 7*D*). We posit that the slight difference between simulation and experiment results from dynamic weight redistribution of the three contacts between the vehicle and membrane during locomotion; the simulation assumes the weight is always evenly distributed among contacts.

Using Speed's Response to Tilt to Avoid Merger of Two Vehicles

Given that unequal mass cars typically collide and cohere after some time, we next sought how we could actively mitigate such attraction. As demonstrated above, reducing vehicle mass can lessen the local deformation field to reduce cohesion, but active variation in this parameter is challenging. Intuitively, one could also control the vehicle to increase speed when it nears a high curvature region, thereby allowing the robot to accelerate out of such a region. We note that such a strategy is interesting because the robots could avoid (or potentially enhance) aggregation solely via local field measurements alone. Such dynamics could be useful for future swarms of sensory-challenged robots (60) moving on highly deformable environments.

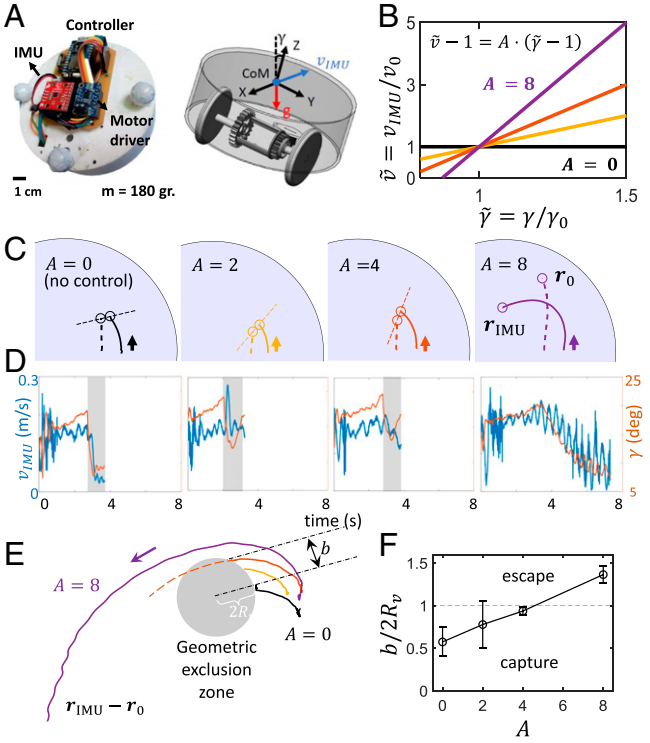

Fig. 8. Speed based on local tilt reduces substrate deformation–induced cohesion. (*A*) A controller, IMU, and DC motor driver are mounted on the speed-controlled vehicle (*Left*; $m \approx 180$ g) that changes speed according to the current tilt angle (*Right*) with the same mechanics as the uncontrolled vehicle. (*B*) Control scheme of the controlled vehicle. The speed v increases with the tilt angle γ to avoid collision. The control parameter A increases from zero (black, no control) to eight (purple). (*C*) The trajectories of the controlled vehicle (solid line) and the uncontrolled vehicle (dashed line) when different magnitudes of control are applied. The relative angle between two vehicles upon collision (dotted line) increases with A. See Movie S6 for movies. (*D*) The evolution of the speed and tilt of the controlled vehicle corresponding to *C*. The shaded regions denote the collisions. (*E*) The trajectories of the IMU-controlled vehicle in the frame of the uncontrolled vehicle. The geometric exclusion zone has a radius twice the radius of a vehicle. In an increasing order of tilt sensitivity $A = 0, 2, 4, 8$, the trajectories get farther and farther away from the uncontrolled vehicle with an increasing margin b. (*F*) Mean and SD of $b/2R_v$ over three trials for different A values. The vehicle eventually avoids the collision when $b/2R_v > 1$.

To test this cohesion mitigation strategy, we recall, from the above section, that, as the distance between the two vehicles decreases, each "feels" the membrane-induced deformation of the other more strongly, and the tilt of both vehicles increases. To measure local tilt angle γ, we added an IMU (internal measurement unit) to the leading vehicle (Fig. 8*A*) and implemented an adaptive speed controller that increased the speed of the leading vehicle as γ, the angle of inclination from the gravity vector measured by the IMU, increased in response to larger substrate deformations. Specifically, the speed of the leading vehicle was designated to be $(v_{\mathrm{IMU}} - v_0)/v_0 = A \cdot (\gamma - \gamma_0)/\gamma_0$, where the tilt sensitivity, A, sets the strength of the coupling between the leading vehicle and the local membrane deformation (Fig. 8*B*).

The speed of the vehicle changes more quickly in response to the tilt when A is larger. We varied A from zero (no control; constant speed) to eight (speed sensitive to tilt angle) to probe the effects of the speed–tilt coupling strength on potential collisions with the trailing vehicle. Fig. 8*C* shows the trajectories of the vehicles starting from the same initial conditions ($r_{\mathrm{IMU}}(0) = 0.6$ m, $r_{\mathrm{passive}}(0) = 0.4$ m, $\theta_{\mathrm{IMU}}(0) = \theta_{\mathrm{passive}}(0) = 90°$, $v_{\mathrm{passive}} = 0.11$ m/s, $v_{\mathrm{IMU}}(0) = 0.15$ m/s, and $\gamma_0 = 15°$) for different A. From the recorded vehicle three-dimensional (3D) position and orientation, we measured the speed and the tilt angle of the leading vehicle as a function of time; these measurements revealed that the controller generated the desired speed variation with tilt (Fig. 8*D*).

The robot's strategy, based solely on local curvature, leads to an ability to avoid collisions without knowing the location of the other vehicle. We observed that, when A was sufficiently large (≥ 4), the leading vehicle was able to successfully avoid collision. Fig. 8*E* shows the relative trajectories of the controlled (leading) vehicle in the frame of the uncontrolled (trailing) vehicle ($\mathbf{r}_{\mathrm{IMU}} - \mathbf{r}_0$). The geometric exclusion zone (with radius equal to $2R_v$) around the uncontrolled vehicle identifies the collision area. If the controlled vehicle enters this area, then a collision with the uncontrolled vehicle has occurred. As A increased, the margin b (i.e., the shortest distance between the controlled vehicle trajectory and the center of the uncontrolled vehicle) increased and eventually became larger than $2R_v$, indicating that the vehicles escaped the collision (Fig. 8*F*). We note that the trajectory of the uncontrolled vehicle ended prematurely when a collision occurred; therefore, we fit it with an ellipse centered at the uncontrolled vehicle to extrapolate the margin b.

Mitigating the Cohesion of Multiple Vehicles

We next sought to discover whether the tilt-based speed control scheme could be effective in merger mitigation in a system consisting of a larger number of agents. Using the same vehicle ($m \approx 180$ g) and membrane as in the previous experiments, simulations of five vehicles without the tilt-based speed control (Fig. 9) resulted in rapid collisions and mergers. However, if the

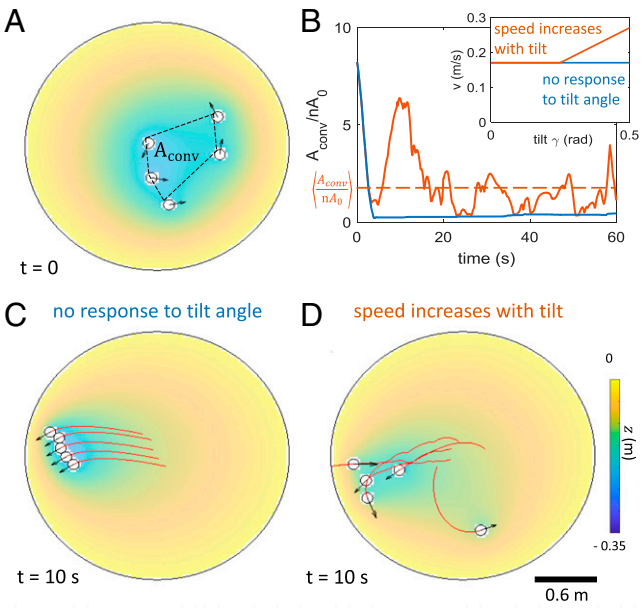

Fig. 9. Increasing speed with tilt helps to avoid mergers in swarms. (*A*) The initial condition used for simulations of five vehicles shown in *C* and *D*. The convex hull of the vehicles (shown by the dotted lines) is used to characterize the proximity of vehicles over time. (*B*) The evolution of the convex-hull area of $n = 5$ vehicles. The evolution with vehicles under speed control is shown in orange. The response of the speed to the tilt angle is shown in *Inset*. The convex area A_{conv} is normalized by the total area of the n vehicles, each with an area of A_0. The orange dashed line shows the time average of A_{conv}/nA_0 at steady state for a single trial. A simulation of five vehicles without speed control is shown in blue. (*C*) Without speed control, the vehicles attract and align with each other in a short time ($t < 10$ s) regardless of their different headings and positions at $t = 0$. (*D*) When the speed control is applied, the vehicles dynamically avoid each other. The snapshot of the vehicles' status at the same time as *C* shows no mergers or alignment of headings. For videos of *C* and *D*, see Movie S7. The red tails show the trajectories of the last 5 s.

speed of the vehicle responds rapidly to its tilt as in Fig. 8, vehicles can dynamically avoid each other.

To characterize the dynamical cohesion among the vehicles, we tracked the convex-hull area (Fig. 9*A*) of the collective. In the case with no speed control, this area decreased to a value close to zero and maintained this value as the vehicles remained stuck to each other (Fig. 9*B* and *C*). However, when sufficient control (tilt sensitivity $\Delta v/\Delta\gamma$) was applied, vehicles starting from the same initial condition as the case with no control (Fig. 9*A*) increased their speed when approaching each other, resulting in a time-dependent convex area with a larger average mean (Fig. 9*B* and *D*). The average area increased with tilt sensitivity $\Delta v/\Delta\gamma$ as shown in Fig. 10*A*.

A full theory incorporating the interplay between the multibody interactions and the vehicle's response to them would be useful in understanding the functional role of this mechanism but is beyond the scope of this paper. However, we can gain qualitative insight by analyzing a special but representative case. Here we consider the stable orbit of n bodies on a perfect ring (Fig. 10*B*, *Inset*). The vehicles can achieve this special mode due to the symmetry of the configuration. The black dashed line in Fig. 10*A* shows that the convex-hull area of this characteristic mode $A_{\text{conv}}^{\text{ring mode}} = \pi r_{\text{ring}}^2$ captures the simulation result qualitatively well. Here, the radius of the stable ring r_{ring} follows $k(r_{\text{ring}}) = v(\gamma(r_{\text{ring}}))^2/r_{\text{ring}}$, where $\gamma = |\nabla z|$. Therefore, r_{ring} is determined by the intersection between the central attraction $k(r)$ and the centripetal acceleration $a_c(r) = v(\gamma(r))^2/r$. When there is no speed control scheme, one of two undesirable outcomes arises: Either 1) $a_c(r)$ does not intersect with $k(r)$ and the vehicles cannot exhibit a stable ring orbit for any r or 2) $a_c(r)$ intersects with $k(r)$ within the geometric exclusion zone. One can find the critical tilt sensitivity $A \propto \Delta v/\Delta\gamma$ by making these two curved lines intersect outside the geometric exclusion zone. This minimal model thus rationalizes why a tilt-based scheme can be used in systems with larger numbers of agents.

We can also interpret the speed control from the metric framework perspective. We first generalize the axisymmetric substrate to a substrate with general landscape z such that a vehicle moving on top of it follows Eqs. **10** and **11** to obtain the temporal and spatial curvature of the metric $\alpha^2 = E^2(1 - v^2 e^{-Cgz/v^2})$, $\Phi^2 = E^2 e^{-Cgz/v^2}(1 - v^2 e^{-Cgz/v^2})$. The metric above reveals that the increase of speed v makes the metric approach (conformal) flatness, since the ratio between the temporal curvature α^2 and spatial curvature Φ^2 approaches unity with a higher speed. The flatter spacetime implies smaller interaction between the vehicles. Thus, our adopted strategy can be viewed as a reduction of interaction by manipulating the effective spacetime metric. A fruitful future direction could be to use such insights to develop controllers for agents to mitigate effects of unexpected environmental perturbations.

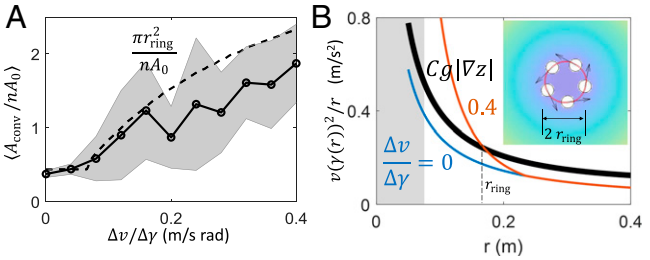

Fig. 10. Speed control and collective merger avoidance. (*A*) Average convex area of the simulated five-vehicle collective increases with the tilt sensitivity (Fig. 9); each point shows the average and SD for 20 different random initial conditions. (*B*) A special mode, the ring mode in which all vehicles move on a circle at a steady state (*Inset*), is used to understand how the characteristic distance depends on the speed control. The black thick line shows the attraction induced by membrane deformation, $Cg|\nabla z|$, and the colored lines show the centripetal acceleration $a_c(r) = v(\gamma(r))^2/r$ required to access the ring mode for cases with control (orange) and without control (blue). The radius of the ring which is given by the intersect of the black thick line and a colored line gives the characteristic area in *A* in a dotted line. The gray shade shows the geometric exclusion zone within which the vehicles collide with each other.

Recently, significant advances of technologies such as small-size, low-cost microrobotics (61) and robust magnetic actuation of microrobot collectives (62) have brought us closer to using active agents for drug delivery (63) and medical operation (64) inside living systems. In these systems where interactions may be mediated through cell membrane and vessels, we posit that our technique of using local information can help prevent undesired clustering of underactuated agents, which will be out of control after the cohesion. Additionally, there are systems wherein well-actuated active agents can benefit from a programmed clustering, because a collective can sometimes accomplish more complicated tasks that an individual cannot. For instance, robots individually incapable of traversing a bumpy landscape can connect with others to collectively overcome obstacles (65). We posit that using local information opposite to our merger avoidance scheme could help form useful aggregates for active agents such as accurately steered microrobot clusters in drug delivery (62, 66).

Conclusions

In this work, we performed a study of the locomotion dynamics of active agents on an elastic substrate with interactions mediated solely by local and global deformation (curvature fields). Experimentally, we studied the dynamics of a single vehicle on a centrally curved elastic surface, revealing nearly ubiquitous retrograde precessing orbits. Guided by the theoretical model based on experimental data, we observed that a reduction in vehicle weight leads to prograde precession. To further test our understanding of the vehicle dynamics and the emergent interactions, we next studied the interaction of two vehicles on a relatively flat membrane (without central depression) with the feature that the time-dependent curvature fields of the vehicle reciprocally govern the robot's trajectories. We observed how increasing the mass ratio between the vehicles led to increased curvature field–mediated cohesion. We then developed a control scheme for the multibody system which mitigated cohesion by using only local sensing and interaction with the environment without knowing the positions of the robots on the membrane. The controller changes the vehicle's speed according to the vehicle's local tilt (indirect measurements of the local curvature field) without knowing the positions of the robots on the membrane. Extending the scheme to multiple vehicles interacting with each other on an arbitrary substrate revealed that our framework and control scheme could be generalized to active-matter systems that consist of a larger number of agents.

Theoretically, to understand the single-vehicle orbital dynamics, we constructed a minimal mechanical model which agreed well with the experimental results and revealed that the vehicle did not simply follow geodesics of the membrane. Inspired by the resemblance of dynamics in our system to those in GR, we wondered whether a differential geometry framework could be of use to better understand features of the system. The active nature of the self-propelled robot allowed us to recast the robot's locomotion dynamics as geodesics of a test particle in an effective spacetime metric. This framework revealed how aspects of the

system (e.g., retrograde precessing orbits) were related to system parameters and allowed us to modify the vehicle mass to change orbital precession from retrograde to prograde; we explore the connections of our robophysical experiments to GR in more depth in ref. 54. To understand the reciprocal curvature field–mediated interaction in a two-robot system, we first generalized the mapping to understand how individual vehicles responded to arbitrary curvature fields. We developed an equation for how the vehicles generated curvature, by showing that the Poisson equation could approximate the shape of the membrane deformed by the masses on it. Solving the Poisson equation analytically demonstrated the origin of forces on the vehicles. Combining the equation of motion for a vehicle on a generalized deformed surface revealed the role of vehicle mass in attraction.

We posit that individuals and swarms of locomoting robots could benefit from discovery and utilization of principles by which agents can interact and communicate by exploiting environmental dynamics (43, 67). Although our system is relatively simple compared to other locomotion and swarm situations in which agents experience field-mediated interactions, the simplicity (such as the linear elasticity in the Poisson equation for the membrane and the acceleration's linear dependence on the local gradient) could make our work serve as a starting point for other terrestrial (and even surface aquatic) systems with more-complex rheological responses (e.g., media with viscous, plastic, and elastic responses). Study of active systems on elastic fields and the differential geometry framework could thus function as a model system and provide tools to robotic studies (12, 68–71) of a broader class of physical (72, 73) systems. For instance, the local curvature could be used as an input in addition to other information such as vision (6, 74, 75) and stress sensing (14, 60, 76) in swarm robotics. Curvature field information could be exploited by robots with limited sensing and control, for example, in lightweight water-walking robots (70, 77) or self-propelled microrobots (78) swarming on fluid membranes (79). Finally, we note that our study is another example of the rich and underexploited intersection of physics and robotics, adding to the list of tools and ideas— for example, gauge theory (80, 81), diffraction and scattering (37, 82, 83), and statistical mechanics (60, 84). We expect that such robophysical studies can help transition robots and swarms from the factory floor into complex natural environments.

Materials and Methods

Vehicle Preparation. The 3D-printed self-propelling differential driven vehicle has a mass of 165 g and a diameter of 10 cm. The vehicle has two active rear wheels ($d_w = 4$ cm) that are connected via a LEGO Technic - Differential Gears 24-16, which allow independent rotation of the wheels (which are separated by 3.6 cm), and one front caster (Pololu ball caster with 3/8 -inch metal ball) for stability. The active wheels are driven by a Pololu 120:1 mini plastic gearmotor (4.5 V, 120 RPM, 80 mA) that provides constant speed (adjusted by potentiometer), with a maximum of 0.32 m/s. The robot is powered by lithium-ion polymer battery (3.7 V, 500 mAh, from Adafruit).

The lighter vehicle is also 3D printed and has a mass of 50 g and a diameter of 7.5 cm. To reduce the weight, we changed the design of the cap of the vehicle by cutting the unused sections that do not have any connectors, battery holder, etc. We used Pololu wheels ($d = 3$ cm), Pololu ball caster with 3/8″ plastic ball, a lithium-ion polymer battery (3.7 V, 150 mAh, and 6 V), a low-power, 0.36 A (Adafruit), micrometal gearmotor (Pololu), and a 5-V voltage regulator (Pololu). The differential mechanism is the same as the heavy vehicle.

The controlled vehicle has the same mechanical structure as the uncontrolled vehicle. An IMU (SparkFun 9DoF IMU Breakout - LSM9DS1) is mounted on top of the robot. We control the speed of the DC motor by controlling the input voltage to the motor using a pulse width modulation signal. The motor control module includes a Particle Photon microcontroller and Adafruit DRV8833 DC motor driver breakout board. The speed of the motor is adjusted as a function of the tilt angle (γ, the angle of inclination from the gravity vector). The relation is given in Fig. 8*B*. The tilt angle is calculated as $\gamma = \arccos a_z / \sqrt{a_x^2 + a_y^2 + a_z^2}$, where $\mathbf{a}$ is the measured acceleration.

Membrane Preparation. The experimental setup consists of a trampoline ($d = 2.5$ m, Dick's Sporting Goods) covered with a four-way stretchable spandex fabric (Rose Brand, 120″ Spandex, NFR). Four-way stretchable refers to the fact that the strain–stress responses in two perpendicular directions are the same, which provides maximum homogeneity.

We adjusted the tension of the fabric homogeneously and then fixed the fabric to the metal frame using custom-created holes and magnets. This adjustment allowed us to perform all the experiments under the same surface conditions. However, because we fixed the fabric manually, there is slight membrane anisotropy overall. The custom-made height controller attached to a steel disk (10 cm in diameter, McMaster) at the center of the setup with magnets. The controller includes a Firgelli linear actuator (6-inch stroke, 35 pounds) and an Actuonix Linear Actuator Control Board that allow the control of the central height via LAC Software. We used a Logitech webcam to take top-view videos of the experiments and used an Optitrack motion capture system (with Flex 13 cameras and Motive software) to track the robot.

Membrane Characterization. We used the motion capture system mentioned above to record the cross-sections of the membrane for different central depressions and compared them with the theoretical solutions to a membrane following the Poisson equation with uniform load from the membrane self-weight $\Delta Z = \lambda^{-1}$. The shape follows well the analytical solution $Z(r; R, R_0) = 1/4\lambda r^2 + C_1(R, R_0) \log r + C_2(R, R_0)$ when proper membrane constant $\lambda = 6.5$ m is applied. This constant is also used for the multivehicle interaction computations. Check *SI Appendix*, section S6 for more details.

Trajectory Collecting. The position and orientation of the infrared reflective markers on the robot are recorded with a motion capture system consisting of five Optitrack Flex 13 cameras with a resolution of 1.3 megapixels/mm^2.

Considering the slight transient decay/expansion of orbit eccentricity (*SI Appendix*, section S2) and the slight physical defect of the membrane at a particular azimuthal angle that shows up every revolution (2π), we evaluate the precession by fitting the trajectory to a model $r(\varphi) = r_c + e^{-\varphi/\tau}\left(A_1 \cos(\varphi + \varphi_1) + A_2 \cos(\omega_{\text{prec}}\varphi + \varphi_2)\right)$ using the least-square fitting with the experiment trajectories. Half-lives of eccentricity are extracted from this model from the characteristic time τ.

Data Availability. Data have been deposited in Zenodo, https://doi.org/10.5281/zenodo.6780486 (85).

ACKNOWLEDGMENTS. We thank Enes Aydin, Mariam A. Marzouk, Alia Gilbert, Maria Jose Serrato Gutierrez, Camila Dominguez, and Steven Tarr for experimental assistance; Andrew Brown for computational assistance; Perrin Schiebel for the suggestion of using differential motor; Andras Karsai, Ram Avinery, and Steven Tarr for proofreading; Zachary Goddard for creating an early version of the vehicle; and Gary Gibbons for encouragement during early stages of the project. Funding for S.L., Y.O.-A., J.M.R., and D.I.G. was provided by the Army Research Office (ARO) grant no. W911NF-21-1-0033 and the MURI award no. W911NF-19-1-0233; funding was also provided by Dunn Family Professorship. P.L. was supported by NSF Grants 1908042, 1806580, and 1550461. G.L. was supported by NASA Grants 80NSSC20K0641 and 80NSSC20K0522.

Author affiliations: [a]School of Physics, Georgia Institute of Technology, Atlanta, GA 30332; [b]Department of Electrical Engineering, University of Notre Dame, Notre Dame, IN 46556; [c]Department of Mechanical Engineering, University of California, Santa Barbara, CA 93106; [d]Walker Department of Mechanical Engineering, The University of Texas at Austin, Austin, TX 78712; [e]Department of Physics, Emory University, Atlanta, GA 30322; and [f]Center for Gravitational Physics, Department of Physics, University of Texas at Austin, Austin, TX 78712

1. H. F. McCreery, Z. A. Dix, M. D. Breed, R. Nagpal, Collective strategy for obstacle navigation during cooperative transport by ants. *J. Exp. Biol.* **219**, 3366–3375 (2016).
2. C. Anderson, G. Theraulaz, J. L. Deneubourg, Self -assemblages in insect societies. *Insectes Sociaux* **49**, 99–110 (2002).
3. C. K. Hemelrijk, H. Hildenbrandt, Schools of fish and flocks of birds: Their shape and internal structure by self-organization. *Interface Focus* **2**, 726–737 (2012).
4. M. Brambilla, E. Ferrante, M. Birattari, M. Dorigo, Swarm robotics: A review from the swarm engineering perspective. *Swarm Intell.* **7**, 1–41 (2013).
5. M. Schranz, M. Umlauft, M. Sende, W. Elmenreich, Swarm robotic behaviors and current applications. *Front Robot AI* **7**, https://www.frontiersin.org/article/10.3389/frobt.2020.00036 (2020).
6. S. J. Chung, A. A. Paranjape, P. Dames, S. Shen, V. Kumar, A survey on aerial swarm robotics. *IEEE Trans. Robot.* **34**, 837–855 (2018).
7. F. Berlinger, M. Gauci, R. Nagpal, Implicit coordination for 3D underwater collective behaviors in a fish-inspired robot swarm. *Sci. Robot.* **6**, eabd8668 (2021).
8. M. C. Marchetti *et al.*, Hydrodynamics of soft active matter. *Rev. Mod. Phys.* **85**, 1143–1189 (2013).
9. J. Aguilar *et al.*, Collective clog control: Optimizing traffic flow in confined biological and robophysical excavation. *Science* **361**, 672–677 (2018).
10. P. Chvykov *et al.*, Low rattling: A predictive principle for self-organization in active collectives. *Science* **371**, 90–95 (2021).
11. J. W. Bush, Pilot-wave hydrodynamics. *Annu. Rev. Fluid Mech.* **47**, 269–292 (2015).
12. D. L. Hu, B. Chan, J. W. M. Bush, The hydrodynamics of water strider locomotion. *Nature* **424**, 663–666 (2003).
13. M. Fruchart, R. Hanai, P. B. Littlewood, V. Vitelli, Non-reciprocal phase transitions. *Nature* **592**, 363–369 (2021).
14. G. Wang *et al.*, Emergent field-driven robot swarm states. *Phys. Rev. Lett.* **126**, 108002 (2021).
15. J. L. Silverberg, M. Bierbaum, J. P. Sethna, I. Cohen, Collective motion of humans in mosh and circle pits at heavy metal concerts. *Phys. Rev. Lett.* **110**, 228701 (2013).
16. A. Cavagna, I. Giardina, Bird flocks as condensed matter. *Annu. Rev. Condens. Matter Phys.* **5**, 183–207 (2014).
17. J. K. Parrish, W. M. Hamner, *Animal Groups in Three Dimensions: How Species Aggregate* (Cambridge University Press, 1997).
18. C. Li, T. Zhang, D. I. Goldman, A terradynamics of legged locomotion on granular media. *Science* **339**, 1408–1412 (2013).
19. J. Aguilar *et al.*, A review on locomotion robophysics: The study of movement at the intersection of robotics, soft matter and dynamical systems. *Rep. Prog. Phys.* **79**, 110001 (2016).
20. T. Li *et al.*, Fast-moving soft electronic fish. *Sci. Adv.* **3**, e1602045 (2017).
21. G. K. Lau, A stunt flying hawk-inspired drone. *Sci. Robot.* **5**, eabe8379 (2020).
22. S. Berman, Q. Lindsey, M. S. Sakar, V. Kumar, S. C. Pratt, Experimental study and modeling of group retrieval in ants as an approach to collective transport in swarm robotic systems. *Proc. IEEE* **99**, 1470–1481 (2011).
23. M. Rubenstein, A. Cornejo, R. Nagpal, Programmable self-assembly in a thousand-robot swarm. *Science* **345**, 795–799 (2014).
24. L. Parolini, A. D. Law, A. Maestro, D. M. A. Buzza, P. Cicuta, Interaction between colloidal particles on an oil-water interface in dilute and dense phases. *J. Phys. Condens. Matter* **27**, 194119 (2015).
25. D. G. Lee, P. Cicuta, D. Vella, Self-assembly of repulsive interfacial particles via collective sinking. *Soft Matter* **13**, 212–221 (2016).
26. D. L. Hu, J. W. Bush, Meniscus-climbing insects. *Nature* **437**, 733–736 (2005).
27. S. Shrivastava *et al.*, Material remodeling and unconventional gaits facilitate locomotion of a robophysical rover over granular terrain. *Sci. Robot.* **5**, eaba3499 (2020).
28. A. S. Baumgarten, K. Kamrin, A general constitutive model for dense, fine-particle suspensions validated in many geometries. *Proc. Natl. Acad. Sci. U.S.A.* **116**, 20828–20836 (2019).
29. A. J. Spence, S. Revzen, J. Seipel, C. Mullens, R. J. Full, Insects running on elastic surfaces. *J. Exp. Biol.* **213**, 1907–1920 (2010).
30. H. Hayati, D. Eager, P. Walker, The effects of surface compliance on greyhound galloping dynamics. *Proc. Inst. Mech. Eng. K J. Multi-body Dyn.* **233**, 1033–1043 (2019).
31. T. A. McMahon, P. R. Greene, The influence of track compliance on running. *J. Biomech.* **12**, 893–904 (1979).
32. D. P. Ferris, M. Louie, C. T. Farley, Running in the real world: Adjusting leg stiffness for different surfaces. *Proc. Biol. Sci.* **265**, 989–994 (1998).
33. D. P. Ferris, K. Liang, C. T. Farley, Runners adjust leg stiffness for their first step on a new running surface. *J. Biomech.* **32**, 787–794 (1999).
34. F. Qian, D. E. Koditschek, An obstacle disturbance selection framework: Emergent robot steady states under repeated collisions. *Int. J. Rob. Res.* **39**, 1549–1566 (2020).
35. S. W. Gart, C. Yan, R. Othayoth, Z. Ren, C. Li, Dynamic traversal of large gaps by insects and legged robots reveals a template. *Bioinspir. Biomim.* **13**, 026006 (2018).
36. C. Li *et al.*, Terradynamically streamlined shapes in animals and robots enhance traversability through densely cluttered terrain. *Bioinspir. Biomim.* **10**, 046003 (2015).
37. P. E. Schiebel *et al.*, Mechanical diffraction reveals the role of passive dynamics in a slithering snake. *Proc. Natl. Acad. Sci. U.S.A.* **116**, 4798–4803 (2019).
38. M. Landolfa, F. Barth, Vibrations in the orb web of the spider *Nephila clavipes*: Cues for discrimination and orientation. *J. Comp. Physiol. A Neuroethol. Sens. Neural Behav. Physiol.* **179**, 493–508 (2004).
39. B. Mortimer *et al.*, The speed of sound in silk: Linking material performance to biological function. *Adv. Mater.* **26**, 5179–5183 (2014).
40. X. Liang, J. Howard, Structural biology: Piezo senses tension through curvature. *Curr. Biol.* **28**, R357–R359 (2018).
41. X. Dong, M. Sitti, Controlling two-dimensional collective formation and cooperative behavior of magnetic microrobot swarms. *Int. J. Rob. Res.* **39**, 617–638 (2020).
42. K. Elamvazhuthi, S. Berman, Mean-field models in swarm robotics: A survey. *Bioinspir. Biomim.* **15**, 015001 (2019).
43. D. Vella, L. Mahadevan, The "cheerios effect." *Am. J. Phys.* **73**, 817–825 (2005).
44. S. Gart, D. Vella, S. Jung, The collective motion of nematodes in a thin liquid layer. *Soft Matter* **7**, 2444–2448 (2011).
45. H. P. Zhang, A. Be'er, E. L. Florin, H. L. Swinney, Collective motion and density fluctuations in bacterial colonies. *Proc. Natl. Acad. Sci. U.S.A.* **107**, 13626–13630 (2010).
46. T. Vicsek, A. Czirók, E. Ben-Jacob, I. Cohen, O. Shochet, Novel type of phase transition in a system of self-driven particles. *Phys. Rev. Lett.* **75**, 1226–1229 (1995).
47. B. Szabó *et al.*, Phase transition in the collective migration of tissue cells: Experiment and model. *Phys. Rev. E Stat. Nonlin. Soft Matter Phys.* **74**, 061908 (2006).
48. F. B. Hoogterp, W. R. Meldrum, Differential torque steering for future combat vehicles. *SAE Trans.* **108**, 575–584 (1999).
49. Y. Chung, C. Park, F. Harashima, A position control differential drive wheeled mobile robot. *IEEE Trans. Ind. Electron.* **48**, 853–863 (2001).
50. J. Wang, Q. N. Wang, L. Q. Jin, C. X. Song, Independent wheel torque control of 4WD electric vehicle for differential drive assisted steering. *Mechatronics* **21**, 63–76 (2011).
51. J. J. Uicker *et al.*, *Theory of Machines and Mechanisms* (Oxford University Press, New York, NY, 2011).
52. A. Gauthier, D. van der Meer, J. H. Snoeijer, G. Lajoinie, Capillary orbits. *Nat. Commun.* **10**, 3947 (2019).
53. M. Pössel, Relatively complicated? Using models to teach general relativity at different levels. *arXiv* [Preprint] (2018). https://doi.org/10.48550/arXiv.1812.11589. Accessed 28 June 2022.
54. S. Li *et al.*, Robophysical modeling of spacetime dynamics. *arXiv* [Preprint] (2022). https://doi.org/10.48550/arXiv.2202.04835. Accessed 28 June 2022.
55. J. B. Hartle, *Gravity: An Introduction to Einstein's General Relativity* (Pearson, 2003).
56. T. Clifton, J. D. Barrow, The power of general relativity. *Phys. Rev. D* **72**, 103005 (2005).
57. G. M. Clemence, The relativity effect in planetary motions. *Rev. Mod. Phys.* **19**, 361 (1947).
58. S. Sarkar, M. Čebron, M. Brojan, A. Košmrlj, Method of image charges for describing deformation of bounded two-dimensional solids with circular inclusions. *Phys. Rev. E* **103**, 053004 (2021).
59. S. Naoz, The eccentric Kozai-Lidov effect and its applications. *Annu. Rev. Astron. Astrophys.* **54**, 441–489 (2016).
60. S. Li *et al.*, Programming active cohesive granular matter with mechanically induced phase changes. *Sci. Adv.* **7**, eabe8494 (2021).
61. M. Z. Miskin *et al.*, Electronically integrated, mass-manufactured, microscopic robots. *Nature* **584**, 557–561 (2020).
62. G. Gardi, S. Ceron, W. Wang, K. Petersen, M. Sitti, Microrobot collectives with reconfigurable morphologies, behaviors, and functions. *Nat. Commun.* **13**, 2239 (2022).
63. D. Jang, J. Jeong, H. Song, S. K. Chung, Targeted drug delivery technology using untethered microrobots: A review. *J. Micromech. Microeng.* **29**, 053002 (2019).
64. S. Yim, E. Gultepe, D. H. Gracias, M. Sitti, Biopsy using a magnetic capsule endoscope carrying, releasing, and retrieving untethered microgrippers. *IEEE Trans. Biomed. Eng.* **61**, 513–521 (2014).
65. Y. Ozkan-Aydin, D. I. Goldman, Self-reconfigurable multilegged robot swarms collectively accomplish challenging terradynamic tasks. *Sci. Robot.* **6**, eabf1628 (2021).
66. B. Yigit, Y. Alapan, M. Sitti, Programmable collective behavior in dynamically self-assembled mobile microrobotic swarms. *Adv. Sci. (Weinh.)* **6**, 1801837 (2019).
67. W. Liu, A. F. Winfield, J. Sa, J. Chen, L. Dou, Towards energy optimization: Emergent task allocation in a swarm of foraging robots. *Adapt. Behav.* **15**, 289–305 (2007).
68. S. Floyd, T. Keegan, J. Palmisano, M. Sitti, "A novel water running robot inspired by basilisk lizards" in *2006 IEEE/RSJ International Conference on Intelligent Robots and Systems*, Y. Liu, Ed. (Institute of Electrical and Electronics Engineers, 2006), pp. 5430–5436.
69. K. Suzuki, H. Takanobu, K. Noya, H. Koike, H. Miura, "Water strider robots with microfabricated hydrophobic legs" in *2007 IEEE/RSJ International Conference on Intelligent Robots and Systems*, E. Grant, Ed. (Institute of Electrical and Electronics Engineers, 2007), pp. 590–595.
70. J. S. Koh *et al.*, Jumping on water: Surface tension-dominated jumping of water striders and robotic insects. *Science* **349**, 517–521 (2015).
71. Y. Chen, N. Doshi, B. Goldberg, H. Wang, R. J. Wood, Controllable water surface to underwater transition through electrowetting in a hybrid terrestrial-aquatic microrobot. *Nat. Commun.* **9**, 2495 (2018).
72. J. W. Bush, D. L. Hu, Walking on water: Biolocomotion at the interface. *Annu. Rev. Fluid Mech.* **38**, 339–369 (2006).
73. Y. Couder, S. Protière, E. Fort, A. Boudaoud, Dynamical phenomena: Walking and orbiting droplets. *Nature* **437**, 208 (2005).
74. A. Weinstein, A. Cho, G. Loianno, V. Kumar, Visual inertial odometry swarm: An autonomous swarm of vision-based quadrotors. *IEEE Robot. Autom. Lett.* **3**, 1801–1807 (2018).
75. O. Y. Sergiyenko, VV Tyrsa, 3d optical machine vision sensors with intelligent data management for robotic swarm navigation improvement. *IEEE Sens. J.* **21**, 11262–11274 (2021).
76. S. Mayya, P. Pierpaoli, G. Nair, M. Egerstedt, Localization in densely packed swarms using interrobot collisions as a sensing modality. *IEEE Trans. Robot.* **35**, 21–34 (2019).
77. J. Zhao, X. Zhang, Q. Pan, "A water walking robot inspired by water strider" in *2012 IEEE International Conference on Mechatronics and Automation* (Institute of Electrical and Electronics Engineers, 2012), pp. 962–967.
78. A. T. Liu *et al.*, Autoperforation of two-dimensional materials to generate colloidal state machines capable of locomotion. *Faraday Discuss.* **227**, 213–232 (2021).
79. T. A. T. Liu, "Colloidal Electronics," PhD thesis, Massachusetts Institute of Technology, Cambridge, MA (2020).
80. A. Shapere, F. Wilczek, Geometry of self-propulsion at low Reynolds number. *J. Fluid Mech.* **198**, 557–585 (1989).
81. R. L. Hatton, Y. Ding, H. Choset, D. I. Goldman, Geometric visualization of self-propulsion in a complex medium. *Phys. Rev. Lett.* **110**, 078101 (2013).
82. J. M. Rieser *et al.*, Dynamics of scattering in undulatory active collisions. *Phys. Rev. E* **99**, 022606 (2019).
83. F. Qian, D. Goldman, "Anticipatory control using substrate manipulation enables trajectory control of legged locomotion on heterogeneous granular media" in *Micro-and Nanotechnology Sensors, Systems, and Applications VII*, T. George, Ed. (International Society for Optics and Photonics, 2015), vol. 9467, pp. 303–314.
84. S. Mayya, G. Notomista, D. Shell, S. Hutchinson, M. Egerstedt, "Non-uniform robot densities in vibration driven swarms using phase separation theory" in *2019 IEEE/RSJ International Conference on Intelligent Robots and Systems (IROS)*, D. Sun, Ed. (Institute of Electrical and Electronics Engineers, 2019), pp. 4106–4112.
85. S. Li, Data for "Field-mediated locomotor dynamics on highly deformable surfaces." Zenodo. https://zenodo.org/record/6780486. Deposited 29 June 2022.